https://doi.org/10.5194/egusphere-2026-2142
Preprint. Discussion started: 27 April 2026

Increasing Sea Surface Temperature Suppresses Primary Marine Aerosol Production

Raymond J. Leibensperger III[1,†,+], Justin D. Hamlin[2,†], Jena K. Herbst[1], Charbel Harb[1,‡], Ke'La A. Kimble[2,§], Meinrat O. Andreae[1,3], Christopher Lee[1], Greg Sandstrom[1], M. Dale Stokes[1], Grant B. Deane[1], Kimberly A. Prather[1,2,*]

[1]Scripps Institution of Oceanography, University of California San Diego, La Jolla, CA, USA
[2]Department of Chemistry and Biochemistry, University of California San Diego, La Jolla, CA, USA
[3]Max Planck Institute for Chemistry, Mainz, Germany
[†]These authors contributed equally to this work
[+]Now at: Institute of Environmental Physics, Heidelberg University, Heidelberg, Germany
[‡]Now at: RTI International, Durham, NC, USA
[§]Now at: California Air Resources Board, Sacramento, CA, USA

Correspondence to: Kimberly A. Prather (kprather@ucsd.edu)

Abstract. Sea spray aerosol (SSA) influences climate through direct and indirect interactions with radiation. However, the magnitudes of these interactions remain poorly constrained, in part due to a lack of understanding of the influences of sea surface temperature (SST) on SSA production. There is no agreed-upon dependence of SSA production on SST despite numerous field, laboratory, and modelling investigations. In this study, these disagreements are addressed through a simple theoretical framework that describes the interfacial processes and contextualizes previous work. Next, we characterize the connection between SST, seawater bubble concentrations, SSA number concentrations, and SSA emission fluxes using measurements in the Scripps Ocean-Atmosphere Research Simulator (SOARS). This isolated ocean-atmosphere interaction system incorporates wind, waves, and SST controls to produce wave breaking under realistic and controlled conditions. In SOARS, increasing SST from 2 to 23 °C suppressed total subsurface bubble concentrations (between 6.17 and 830 μm) by a factor of 1.5, SSA number concentrations (between 0.008 and 20 μm) by a factor of 3, and SSA accumulation mode emission flux by a factor of 4. Using these trends, we derive SST-dependent number and mass emission flux correction factors for SSA source functions in climate models. While prior studies report both increases and decreases with SST, these controlled wind-wave-SST experiments demonstrate that increasing SST suppresses SSA production. Resolving this SST dependence is critical, as it directly alters marine aerosol burdens, cloud condensation nuclei, and radiative forcing, and provides a needed constraint missing from current parameterizations.

1 Introduction

Since the 1980s, global surface temperatures have increased at an estimated 0.2 °C per decade, accelerating to 3.5 °C per decade since about 2010 (Foster and Rahmstorf, 2026; Hansen et al., 2006). More than 90% of this warming is estimated to be absorbed by the oceans, with warming concentrated at the surface (Llovel and Terray, 2016; Willis et al., 2004), altering the ocean-atmosphere interface (OAI) (Resplandy et al., 2019). Aerosols produced at the OAI play an important role in mitigating global warming directly by scattering solar radiation and indirectly by influencing the micro- and macro-physical properties of clouds (Albrecht, 1989; Haywood and Boucher, 2000; Intergovernmental Panel on Climate Change (IPCC), 2023; Lohmann and Feichter, 2005; Twomey, 1980). With 71% of Earth's surface covered by oceans, contributions from both natural and anthropogenic marine aerosols are active areas of study (Lewis and Schwartz, 2004; O'Dowd and De Leeuw, 2007; Quinn et al., 2015; Russell et al., 2023).

Sea spray aerosols (SSA) are the most ubiquitous natural marine aerosol, responsible for an estimated mass flux between 3 and 30 Pg yr^{-1} (Glią et al., 2021; Grythe et al., 2014; de Leeuw et al., 2011; Lewis and Schwartz, 2004). SSA are produced during wave breaking, where air is entrained beneath the ocean surface to form bubbles. These subsurface bubbles rise and produce surface whitecaps, which emit SSA primarily through film and jet drop production (Bird et al., 2010; Brasz et al., 2018; de Leeuw et al., 2011; Lewis and Schwartz, 2004; Quinn et al., 2015). Additionally, SSA are also produced when surface wind speeds exceed between 7 and 11 m s^{-1}, wherein spume drops are ripped directly from the top of wave crests (Andreas et al., 1995; Mehta et al., 2019; Veron et al., 2012), however, this process is not the focus of the current study.

There is no consensus on how sea surface temperature (SST) influences SSA emissions. Quantifying the role of SST on SSA emissions has been the focus of numerous field measurements, laboratory measurements, and first-principles theories. The review by Song et al., (2023) comments on the conflicting results of previous studies, summarized in Table S1. Some studies report a negative correlation (Lehahn et al., 2014; Markuszewski et al., 2024; Nielsen and Bilde, 2020; Sellegri et al., 2023; Sofiev et al., 2011), whereas others report a positive correlation (Forestieri et al., 2018; Grythe et al., 2014; Hu et al., 2024; Liu et al., 2021; Ovadnevaite et al., 2014). Non-monotonic relationships have also been reported (Christiansen et al., 2019; Hu et al., 2024; Jaeglé et al., 2011; Mårtensson et al., 2003; Saliba et al., 2019; Salter et al., 2014, 2015; Zábori et al., 2012; Zinke et al., 2022), underscoring the complex relationship between SSA and SST.

The use of different breaking wave proxies in laboratory studies complicates the interpretation of results in previous studies. The importance of accurate SSA generation mechanisms cannot be overstated (Collins et al., 2014; Fuentes et al., 2010; Lewis and Schwartz, 2004; Prather et al., 2013). A fundamental limitation of previous laboratory studies, and a plausible explanation for conflicting results, is the absence of controlled winds. This study uses the Scripps Ocean-Atmosphere Research Simulator (SOARS) to control SST, wave state, and wind speed to characterize SSA emissions at varied SSTs. While previous laboratory proxies offer valuable insights into the dependence of SSA production on SST, SSA production from representative wind-wave interactions will alter bubble plumes, and thus SSA emissions. Measurements in SOARS can be used to correct simulated SSA emissions in Earth System Models (ESMs), which typically incorporate a positive correlation with SST (Grythe et al., 2014; Jaeglé et al., 2011; Song et al., 2023).

https://doi.org/10.5194/egusphere-2026-2142
Preprint. Discussion started: 27 April 2026

This study employs a multi-pronged investigation of the SST dependencies of marine aerosol production through the conceptualization of a common framework (Sect. 3.1), followed by SST-dependent measurements of whitecap fractions and subsurface bubble populations (Sect. 3.2), SSA number concentrations (Sect. 3.3), a comparison of SSA and subsurface bubble concentrations (Sect. 3.4), and SSA emission fluxes (Sect. 3.5). These findings culminate in the creation of temperature-dependent correction factors derived from the first wind-wave controlled SST experiments for direct integration into climate models (Sect. 3.6).

2 Materials and Methods

2.1 Sea Spray Aerosol Generation in SOARS

The SOARS instrument is located within the Hydraulics Laboratory at the Scripps Institution of Oceanography at the University of California San Diego in La Jolla, CA, USA. SOARS is a combined wave channel (36 m x 2.4 m x 2.4 m) and recirculating wind tunnel with an air-backed paddle at one end generating user-defined wave fields and a partially submerged ramp at the other end to absorb and dissipate wave energy. Two experiments were conducted from 11 February to 1 March 2024 using SOARS to quantify the effects of increasing SSTs on SSA production. In each experiment, water temperatures in SOARS, hereafter referred to as SSTs for simplicity, were controlled across a ~20 °C range (Figure 1a). The first experiment (“Cooling”), monotonically decreased SST each day, while the second experiment (“Warming”) did the opposite. Both experiments utilized the same seawater, collected from the Ellen Browning Scripps Memorial Pier (La Jolla, CA; 32°52‘1" N; 117°15'26” W). The seawater was filtered through 10 μm mesh filters prior to experimental runs to reduce the influence of biology, pollution, and surface-active chemistry on SSA emissions (Kimble et al., 2026). Once filled, the SOARS water was continuously filtered through 1 μm mesh filters and UV sterilizers (λ = 264 nm). SSA was produced by combining a wave field, where every fifth wave crest was a gently spilling breaker along the length of the channel, with a 10 m extrapolated wind speed (U_{10}) of 11 m s^{-1}. This wind speed and wave field pairing were chosen to replicate equilibrium seas not under high winds, with more discussion included in an accompanying manuscript.

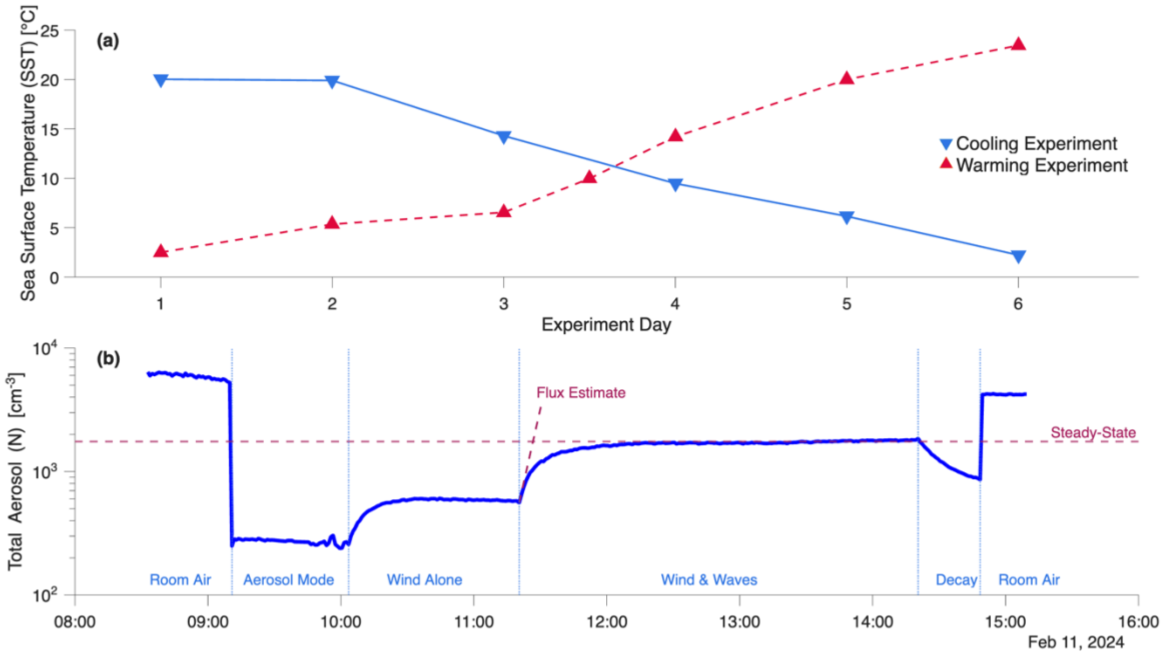

Figure 1: (a) Sea surface temperature for each experimental day and (b) total aerosol number concentrations during a representative experimental day (11 February 2024, cooling experiment day 1).

A representative experimental day of operating conditions is shown in Figure 1b, broken down into six measurement periods: 1) Room Air, 2) Aerosol Mode, 3) Wind Alone, 4) Wind & Waves, 5) Decay, and 6) Room Air. Representative particle number size distributions (PNSDs) from each period on three days with equivalent SSTs are displayed in Figure S1. Room air measurements from the beginning and end of each day characterize background aerosol concentrations in the Hydraulics Laboratory. Aerosol mode, wherein the SOARS headspace is cycled through high efficiency air particulate (HEPA), clean carbon MERV 16, and potassium permanganate filter banks, is operated for ~45 minutes, removing over 85% of background particles. Once aerosol concentrations are sufficiently low, U_{10} winds are set to 11 m s^{-1} for ~45 minutes (Wind Alone mode) to remove particles adhered to channel walls and create a stable headspace before SSA generation. During Wind & Waves mode, a wave field is generated with a peak wave height of 0.42 m, enabling measurements of SSA concentrations and flux estimates (Sect. 2.3–2.4, annotated by the magenta dashed lines in Figure 1b). SSTs and salinities (Table S2) are measured during Wind & Waves using a YSI Pro 30 (YSI Inc., Yellow Springs, OH). Following Wind & Waves, waves are stopped to allow for estimates of aerosol loss rates during the Decay period, not analysed in this study.

2.2 Sea Spray Aerosol Sampling

Primary SSA was sampled through two stainless steel inlets (2.27 m length; 10 mm ID) positioned 32 m downstream of wave generation and angled in the direction of wave breaking (Fig. S2). The two parallel sampling systems had total flow rates of 6.2 and 2.6 L min^{-1}. The sampled SSA was dried (relative humidity < 20 %) by passing sample flows through homemade silica diffusion dryers to minimize the influence of hygroscopic growth on particle size. The sampling system produces size-dependent particle losses, which introduce uncertainty into the SSA measurements. The Particle Loss Calculator (PLC, described by Von Der Weiden et al. (2009)) estimated sampling efficiency corrections for each instrument and SOARS Wind & Waves conditions (Fig. S3).

2.3 Sea Spray Aerosol Measurements

Submicron SSA (D < 1 µm) were measured using a Scanning Mobility Particle Sizer model 3938 (SMPS; TSI Inc., Shoreview, MN) and Spider-MAGIC model 800 (SM; Aerosol Dynamics Inc., Berkeley, CA). The SMPS consisted of a 0.0701 cm impactor, model 3088 advanced aerosol neutralizer, model 3081A differential mobility analyser (DMA) operated in negative polarity, and a model 3789 condensation particle counter (CPC). Aerosol and sheath flow rates of 0.6 and 3 L min^{-1} enabled measurements of particles with mobility diameters (D_m) from 0.013 to 0.835 µm every minute, with a scan time of 45 seconds and a purge time of 15 seconds. The SM, introduced by Amanatidis et al. (2020, 2021) consisted of a Po-210 radioactive charge conditioner (500 µCi; NRD, Grand Island, NY), Spider DMA operated with alternating up and down dual polarity scans, and a Moderated Aerosol Growth with Internal water Cycling (MAGIC) CPC (Hering et al., 2019). Aerosol and sheath flow rates of 0.3 and 0.9 L min^{-1} enabled measurements of particles with D_m from 0.008 to 0.42 µm. The SM scan time was approximately 30 seconds for a unidirectional, single polarity voltage ramp, with a complete scan over both polarities and each voltage ramp direction in about two minutes.

Supermicron SSA (D > 1 µm) were measured using optical measurement techniques. An Aerodynamic Particle Sizer model 3321 (APS; TSI Inc., Shoreview, MN) measured particles with aerodynamic diameters (D_a) from 0.52 to 20 µm with a total flow rate of 5 L min^{-1}. An Optical Particle Sizer model 3330 (OPS; TSI Inc., Shoreview, MN) measured particles with optical diameters (D_o) from 0.3 to 10 µm with a sample flow rate of 1 L min^{-1}. The APS and OPS were both operated at one-minute resolution, synchronized with the submicron measurements.

Particle number size distributions (PNSDs) from the three measurement techniques were converted to dry, physical diameters ($D_{p,\ dry}$) assuming spherical particles. Equations 1 and 2 have been used previously to combine mobility and aerodynamic measurements (Collins et al., 2014; Lewis and Schwartz, 2004; Stokes et al., 2013), where D_m is assumed to be equal to $D_{p,\ dry}$ (Eq. 1) and D_a is converted to $D_{p,\ dry}$ by estimating the effective density (ρ_{eff}) based on relative humidity, assuming a mixture of pure NaCl salt and water following Fig. 7 from Lewis and Schwartz (2004), and a reference density (ρ_0) of 1 g cm^{-3} (Eq. 2). Finally, D_o is assumed to be equal to $D_{p,\ dry}$ (Eq. 3), as previous measurements of the refractive index of dried SSA (m_{SSA} = 1.533) by Liu et al. (2023) were found to be reasonably close to that of the calibration aerosol, polystyrene latex spheres (m_{PSL} = 1.588).

$$D_{p,\ dry} = D_m, \qquad (1)$$

$$D_{p,\ dry} = \frac{D_a}{\sqrt{\frac{\rho_{eff}}{\rho_0}}}, \tag{2}$$

$$D_{p,\ dry} = D_o, \tag{3}$$

Total particle concentrations from 5 nm to 2.5 µm were measured using a MAGIC CPC (Aerosol Dynamic Inc., Berkeley, CA). The MAGIC CPC served as the reference instrument for room air and in-channel number concentrations shown in Figure 1b. Loss-corrected data from the SMPS and APS were merged using a 2:1 weighting factor favouring the SMPS in the overlapping size range due to low APS counting efficiency below 0.9 µm (Peters and Leith, 2003; Pfeifer et al., 2016). The SM and OPS PNSDs were similarly merged, but with a 1:1 weighting due to a smaller overlapping size range and insufficient data on instrument counting efficiency in this region. Total SSA numbers (N) were estimated by integrating the PNSD. By assuming spherical particles, we also transform the PNSDs into distributions of surface area and volume, similarly estimating total surface area (S) and volume (V) by integrating the respective distributions.

For most of the analysis, measurements were condensed into 5 °C bins covering SSTs from 0 to 25 °C. Since this process reduces the number of points to only n=5, we performed an uncertainty-weighting analysis. Applying this weighting factor (Eq. S1) did not dramatically adjust our regressions but increased confidence in our findings (Figure S4). More information on this analysis and a comparison between the weighted and non-weighted number concentrations can be found in the Supplemental Information.

2.4 Production Flux Measurements

Estimates of particle number flux distributions (PNFDs) utilized three methods to account for size-dependent influences on SSA production. First, submicron PNFDs were estimated by applying a linear regression to the SSA number concentration time series during the initial 5 minutes of Wind & Waves mode. This method assumes minimal losses based on the sufficiently long residence times of submicron SSA. Second, supermicron SSA between 1 and 4 µm PNFDs were estimated for each size bin by applying a power law regression fit to the entire time series of SSA number concentrations during Wind & Waves mode. For SSA above 4 µm, steady state was reached within the first minute of sampling due to short residence times. For these supermicron SSA, first-order loss rates were estimated during the Decay mode. A well-mixed reactor was assumed to estimate the production flux equivalent to the product of the steady state concentration and first-order loss rate. Particle mass flux distributions (PMFDs) were estimated by multiplying the PNFD by the spherical volume of SSA at each size and assuming a constant density of 2.2 g cm^{-3} (Brock et al., 2019; Wu et al., 2020). Total number fluxes (F_N) and total mass fluxes (F_M) are the result of integrating the PNFDs and PMFDs.

2.5 Bubble Measurements

Whitecap fractions (WCF) in SOARS were measured via image analysis of wave breaking. During Wind & Waves mode, a Nikon D3200 SLR camera (shutter speed 1/500 s, f-stop 5.6, ISO 1600) photographed whitecaps from atop the SOARS lid.

Each sequence occurred over 12.5 seconds, captured 27 images, and was repeated for at least ten breaking events. The field of view, located 11 m downwind of wave generation, was illuminated through the side wall of the channel. Background images of still water were subtracted from whitecap images to eliminate the influence of lighting inconsistencies and image deformation. Whitecaps in the resulting images were identified using a thresholding technique. An average WCF value was computed across breaking events for each temperature. Measurements below SSTs of 6 °C were not possible due to significant fogging of the SOARS lid.

Total subsurface bubble concentrations (n) with radii from 6.17 to 830 µm were measured acoustically. Measurements were based on Vagle and Farmer (1998), employing two submerged transducers. The first emits sound between 80 and 250 Hz during a 3-second interval, while the second receives the attenuated signal. Signal attenuations at several frequencies are inverted into a bubble size distribution using the resonant bubble approximation (Czerski, 2012). The bubble size distribution was then integrated across the size range to estimate total concentrations.

3 Results and Discussion

3.1 A Simple Framework of SSA Production

To begin, we present a simple framework to contextualize our measurements and summarize the current understanding of SSA production, using notation that is conserved throughout the remainder of this work. The change in net amount of SSA at a given $D_{p,\,dry}$ that enters the atmosphere over a given ocean area (N, [$\#_{SSA}$, m^{-2} μm^{-1}]) produced from surface bubbles (ñ, [$\#_{bubble}$ m^{-2} μm^{-1}]) over time is characterized by Eq. 4:

$$\frac{dN}{dt} = \int_{r_{min}}^{r_{max}} E * B * \tilde{n} * dr - D_1 * N, \tag{4}$$

Where E is the number of SSA emitted per bubble [$\#_{SSA}$ $\#_{bubble}^{-1}$], B is the burst rate of surface bubbles [s^{-1}], r is the bubble radius [µm], and D_1 is the deposition rate of SSA [s^{-1}].

Based on previous work, we expect that E, B, and ñ will vary as a function of SST due to changes in seawater and bubble properties (Nielsen and Bilde, 2020; Sellegri et al., 2023; Song et al., 2023). These properties include: the bubble film drainage (φ), bubble film thickness (η), bubble film brittleness (β), air entrainment (ε), kinematic viscosity (ν), surface tension (γ), and the solubility of gases (κ). The number of SSA ejected per burst bubble (E) is known to be proportional to η and β while inversely proportional to φ and ν, and can vary by a factor of 58 over an SST range of 0 to 19 °C (Nielsen and Bilde, 2020):

$$E \propto \frac{\eta\beta}{\varphi\nu}, \tag{5}$$

The number of SSA ejected per bubble is different for film and jet drop production, and thus dependent on $D_{p,\,dry}$ of SSA and r of bubbles. Surface bubble burst rate (B) is inversely proportional to surface tension (Nielsen and Bilde, 2020; Song et al., 2023):

$$B \propto \gamma^{-1}, \qquad (6)$$

The surface bubble concentrations (ñ) will vary non-linearly with SST, depending on the indirect effects of water properties, following the relations given in Eqs. S2-S8. Further, subsurface bubbles interact with one another, altering their size-dependent concentrations and likely influencing SSA production (Jiang et al., 2024).

The lack of consensus on the SST dependence of SSA production stems in part from the competing physical processes described in Eqs. 4–6. For example, increasing SST simultaneously enhances bubble burst rates (Eq. 6) and reduces the number of SSA ejected per bubble (Eq. 5), and these opposing effects are functions of bubble size. Without isolating and quantifying each process independently, observations of SSA production will reflect the sum of these competing influences, making it difficult to attribute trends to any single mechanism (Sellegri et al., 2023; Sofieva et al., 2022). Characterizing the relationship between surface and subsurface bubbles with changing SST is therefore a critical first step toward disentangling these effects.

3.2 Surface and Subsurface Bubbles

Whitecap fractions (WCFs) were measured to estimate the effect of changing SST on the surface expression of subsurface bubble plumes at SSTs above 6 °C (Sect. 2.5). In Figure 2a, no clear dependence is seen between WCF and SST, which is consistent with previous findings (Jia and Zhao, 2019; Liu and Yang, 2022). On the other hand, a previous laboratory study using plunging waterfalls found an increase in air entrainment and surface foam with increasing SSTs over a similar range (6 to 30 °C) (Callaghan et al., 2014). While these results approximately align with the warming results in Figure 2a, our laboratory proxy utilizes wind-wave interactions, likely contributing to the differing results during the cooling experiment.

Subsurface bubble concentrations (n) provide additional insight into how SST modifies the OAI. Figure 2b shows that n decreased by a factor of 1.5 over our SST range, regardless of whether the SST was increasing or decreasing, and the trend is captured by a linear fit ($R^2 = 0.83$). These results show the same trend as the work of Thorpe et al. (1992), who found that n decreased by 50% for every 10 °C increase in SST over the bubble-size range of 5 to 145 µm. However, our observed decrease in n, 12.5% per 10 °C, is lower and may reflect the larger size range measured here (6.17 to 830 µm). Notably, this decrease in subsurface bubble concentrations does not correspond to a clear change in WCF, different from the consistent findings of Callaghan et al. (2014). This suggests that SSA production under wind-wave interactions may be governed by processes occurring beneath the surface (Chu et al., 2025) or by bubbles smaller than 6 µm.

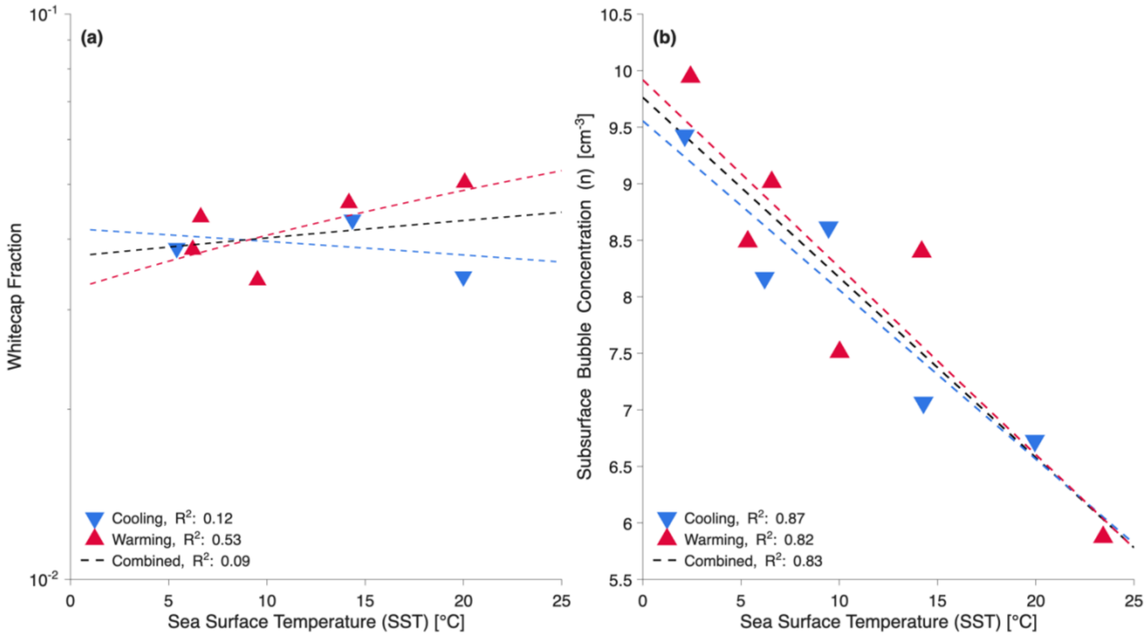

Figure 2: (a) Whitecap fraction and (b) subsurface bubble concentrations as a function of SST.

3.3 Particle Number Size Distributions

Mean PNSDs were calculated during the last hour of each Wind & Waves run and binned in 5 °C increments from 0 to 25 °C. Increasing SST from 2 to 23 °C produced a clear suppression of submicron SSA concentrations (Figure 3), consistent with two independent findings: the diffuser experiments of Christiansen et al. (2019) and the plunging jet measurements of Salter et al. (2015). However, important differences emerge when comparing details across methods. The diffuser-generated PNSDs exhibit mode diameters approximately 50 nm smaller than ours, a discrepancy attributable to differing SSA generation mechanisms. The plunging jet produces mode diameters like ours but yields a U-shaped SST dependence in the submicron regime. These method-dependent inconsistencies reinforce the critical importance of representative SSA production mechanisms (Collins et al., 2014). By generating SSA through realistic wind-wave interactions, SOARS minimizes the artifacts introduced by other laboratory proxies, lending greater confidence to the monotonic suppression observed here for submicron SSA. These trends are further corroborated by independent PNSD measurements from the SM-OPS system (Figure S5, Table S3).

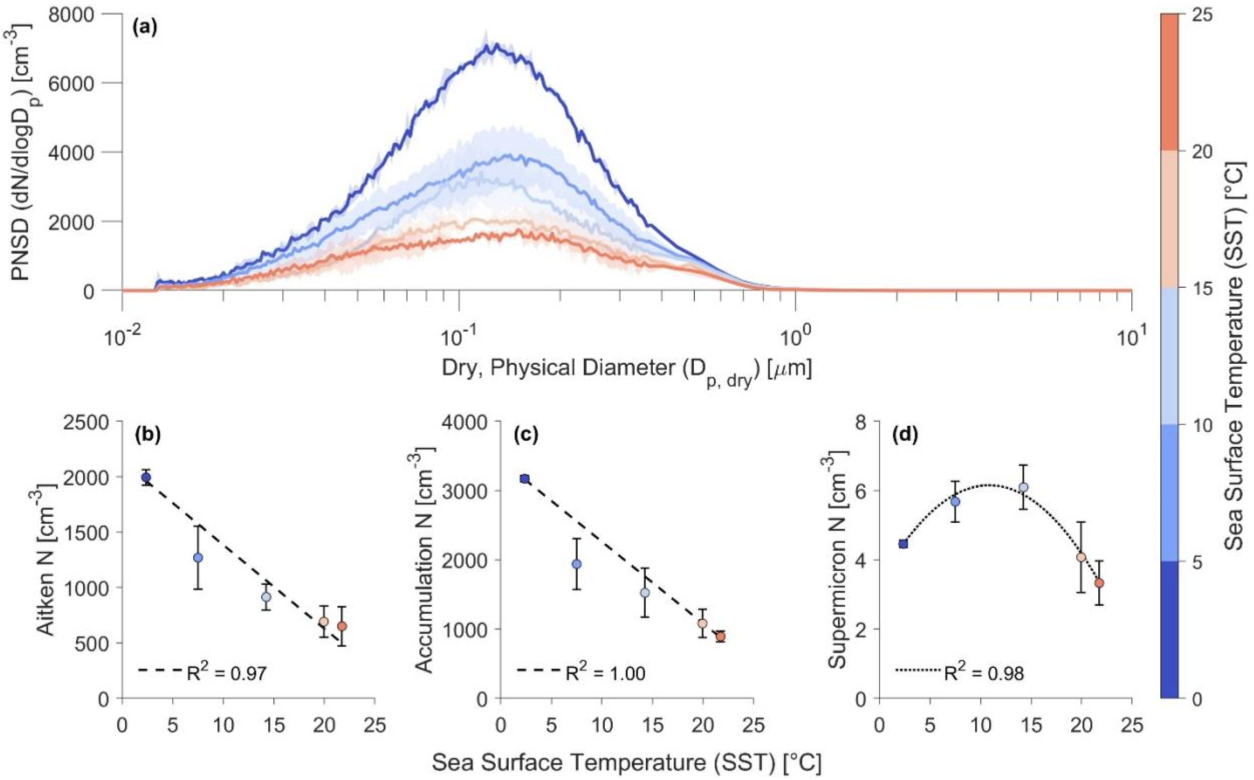

Figure 3: (a) Mean PNSDs for five SST ranges measured by the SMPS-APS. Shaded regions indicate one standard deviation of the mean PNSD. (b) Total Aitken, (c) accumulation, and (d) supermicron mode number concentrations. The error bars in b-d indicate one standard deviation.

Beyond the overall suppression in number concentration, we evaluated whether SST also shifts the shape of the PNSD by examining the temperature dependence of geometric mean diameter (D_g), geometric standard deviation (σ_g), and mode diameter (D_{mode}) (Figure S6). None of these parameters exhibit a clear trend with SST, in contrast to the strong linear decrease observed in total number (N). This indicates that increasing SST reduces the amount of SSA produced without substantially altering the size distribution. The potential for SST to modulate the chemical composition and mixing state of emitted SSA, a subtler effect that would not be captured by these bulk size metrics, is the focus of ongoing single particle analysis in our group to be discussed in a forthcoming manuscript.

Integrated number concentrations over three size ranges clarify size-dependent relationships with SST that are not captured by evaluating the complete PNSD. Suppression of SSA with increasing SST for both Aitken ($0.02 < D_{p,\,dry} < 0.1$ μm) and accumulation ($0.1 < D_{p,\,dry} < 1$ μm) modes is well represented by a linear regression ($R^2 \geq 0.97$, Figure 3b-c). On the other hand, supermicron SSA exhibit a non-linear relationship with SST, which is well represented by a quadratic regression ($R^2 = 0.98$). This suggests a mechanistically driven (i.e., film vs. jet drop) size-dependent shift in production and indicates that increasing SSTs have a complex influence on the resulting SSA.

A tri-modal log-normal fit was applied to the coldest and warmest PNSDs to further characterize the changes in the modal distributions as a function of SST (Figure 4, Table S4). From the lowest to the highest SSTs, the greatest change occurs in the accumulation mode number concentration, which decreases by 75%. Beyond a decrease in magnitude, each mode experiences slight increases in D_g and σ_g. Aitken mode concentrations decrease by 35%, D_g increases by 22%, and σ_g increases by 4%. The accumulation mode N decreases by 75%, D_g increases by 18%, and σ_g increases by 1%. The coarse mode N decreases by 36%, D_g increases by 2%, and σ_g increases by 5%. The minor changes in D_g and σ_g again suggest SST primarily influences the number of SSA at steady state rather than the shape of the distribution.

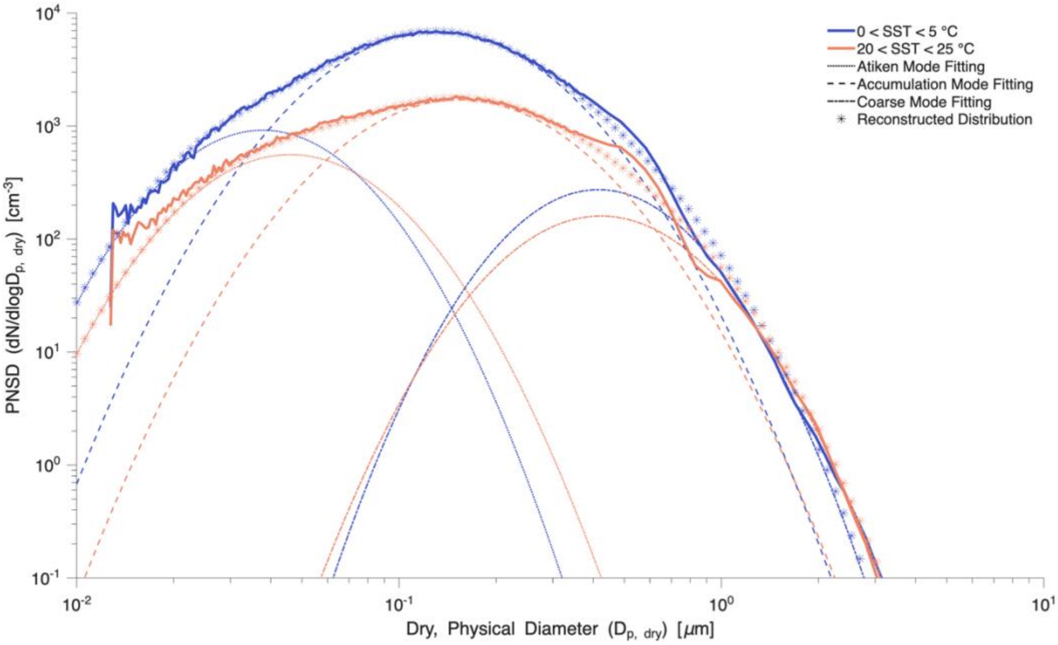

Figure 4: Average PNSD for the coldest and warmest binned SSTs. Each is decomposed into three log-normal modes and reconstructed.

The influence of SST on SSA extends beyond suppression of number concentrations to suppression of higher-order moments of the size distribution. Figure 5 shows that increasing SST drives a decrease in total SSA number, surface area, and volume by more than 50%, across the SST range of 2 to 23 °C. All three moments exhibit strong, negative correlations with SST, which are well represented by linear regressions ($R^2 \geq 0.98$).

https://doi.org/10.5194/egusphere-2026-2142
Preprint. Discussion started: 27 April 2026

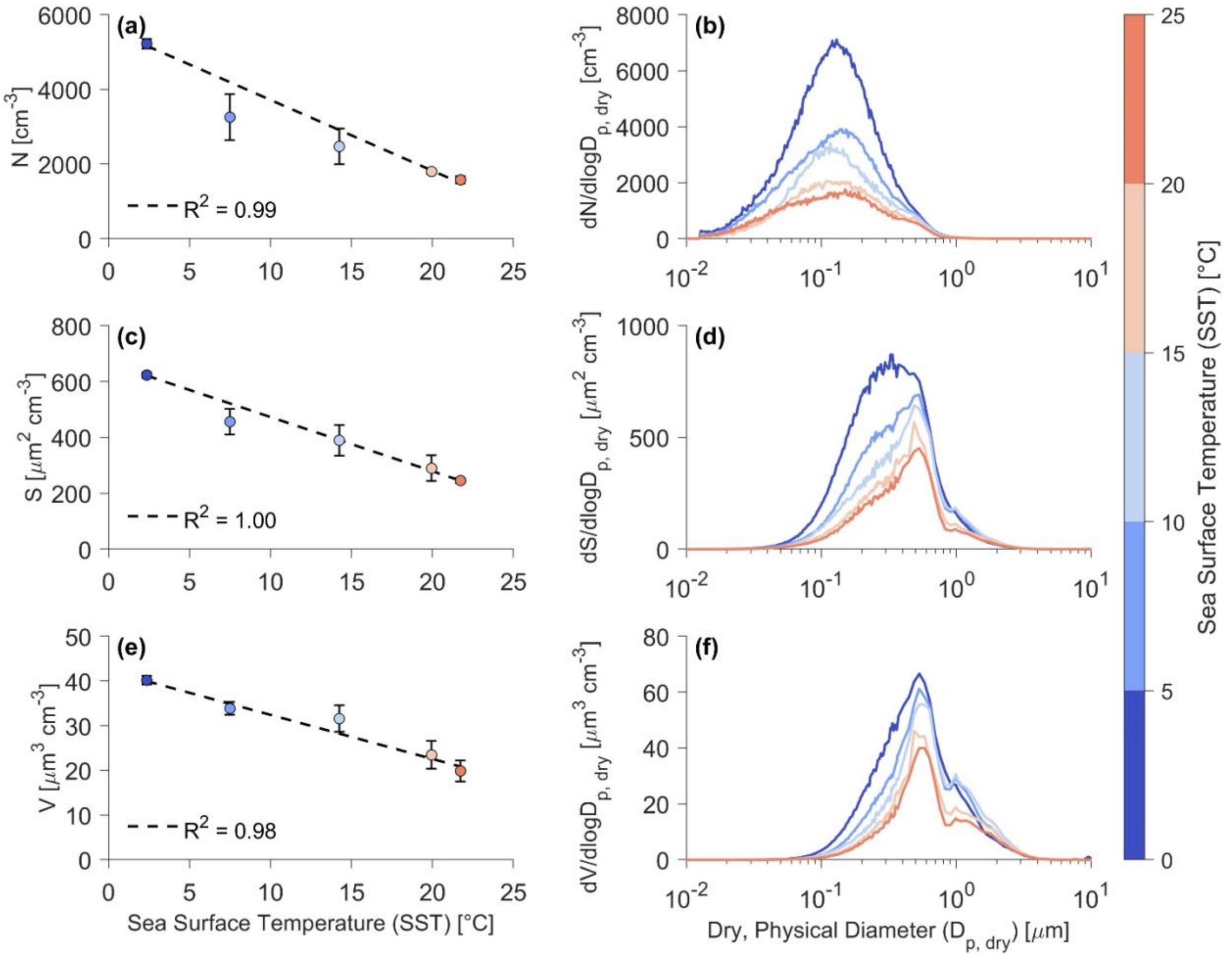

Figure 5: (a) Total number, (c) surface area, and (e) volume of SSA in SOARS for each temperature range, with a dashed line representing a linear least squares best fit line. (b) Number, (d) surface area, and (f) volume size distribution for each temperature range.

The higher-order moments of the size distribution reveal a structural shift that the number distribution alone does not capture (Figure 5). As SST increases from 2 to 7 °C, the surface area distribution transitions from a broad, log-normal mode centred near 0.3 µm to a sharper mode at 0.55 µm, which then persists across all higher SSTs (Figure 5d). The volume distribution undergoes a parallel transition, with a secondary mode emerging near 1 µm over the same temperature range (Figure 5f). Although this secondary mode falls near the SMPS-APS merging point, it also appears in the SM-OPS PNSDs (Figure S5) where merging occurs at 0.4 µm, confirming it is not an artifact of measurement stitching. These modal shifts are also present in the probability density functions of the number, surface area, and volume of the coldest and warmest SSTs (Figure S7).

These shifts carry direct implications for climate; particle surface area underpins several modelling parameterizations for ice nucleating particle concentrations (DeMott et al., 2016; Moore et al., 2022; Phillips et al., 2008), so a redistribution of SSA

https://doi.org/10.5194/egusphere-2026-2142
Preprint. Discussion started: 27 April 2026

surface area into larger sizes could alter the available sites for ice nucleation and, in turn, the abundance of ice and mixed-phase clouds. Simultaneously, the suppression of SSA volume combined with shifts in mode diameter could reduce direct scattering of solar radiation, potentially enhancing poleward heat transport as described by Kay et al. (2016).

The abruptness of these transitions between 2 and 7 °C, followed by relative stability at higher SSTs, points to a possible physicochemical threshold rather than a gradual scaling with temperature. One potential explanation is the influence of marine gels. Despite water treatment to minimize biological contributions (Sect. 2.1), dissolved organic matter and its gel-phase products can persist. The presence of marine gels is well documented in arctic regions, dominating CCN populations (Dall'Osto et al., 2025; Orellana et al., 2011, 2021). Since the gels are temperature sensitive, with significant hydrodynamic diameter growth over the SST range covered here (Chang et al., 2022; Verdugo, 2012), they are likely to become most prevalent in the seawater (and therefore enriched in SSA) at the coldest SSTs. If this hypothesis is true, the resulting organic coating would produce more spherical particles with a more idealized optical response in the size measurements, consistent with the narrow, more uniform distributions at low SSTs seen above. Ongoing single particle compositional analysis will directly test this hypothesis.

3.4 Connecting SSA and Bubble Concentrations

We compare SSA concentrations to subsurface bubble concentrations to contextualize and understand our measurements of SSA number concentrations (Figure 6). The submillimetre subsurface bubble concentrations are likely to be related to jet droplet production, controlling supermicron SSA production and up to 43% of submicron SSA production (Wang et al., 2017). However, the highest correlations occur between the accumulation mode SSA and subsurface bubbles ($R^2 = 0.99$, Figure 6b). More work is needed to understand the non-linear processes connecting changing SSTs to SSA production via size-dependent bubble processes. This analysis provides a cursory look into the temperature-dependent relationship between subsurface bubbles and SSA.

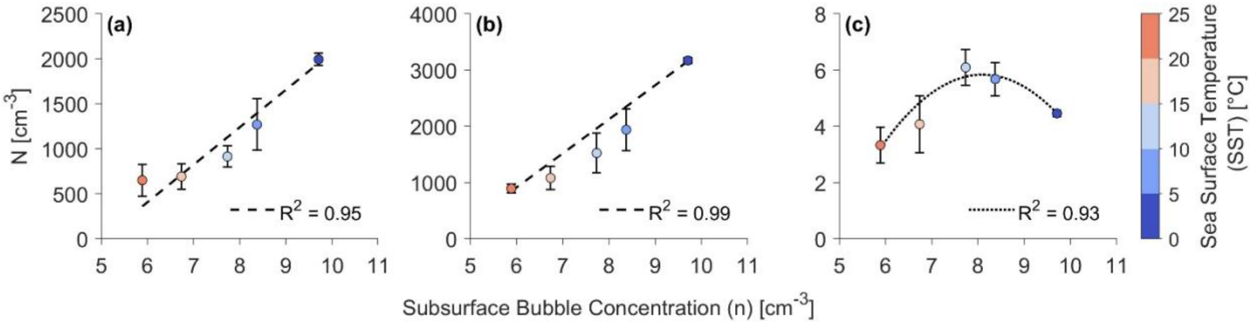

Figure 6: Comparison of SSA total number (N) to subsurface bubble concentrations (n), separated by SSA mode: (a) Aitken, (b) accumulation, and (c) supermicron. Weighted least squares regression and resulting best fit lines are shown for linear (dashed) and quadratic (dotted) fits.

https://doi.org/10.5194/egusphere-2026-2142
Preprint. Discussion started: 27 April 2026

While SSA production has been investigated with various breaking wave analogues in the laboratory (Bowyer et al., 1990; Forestieri et al., 2018; Salter et al., 2014), experiments on SSA production should be conducted with an accompanying emphasis on understanding the dynamics and evolution of the bubble plume, similar to Callaghan et al., (2014). The structure of the subsurface bubble plume is governed by the fluid dynamics within the entire water column, which is dependent on winds and waves (Crawford and Farmer, 1987). The air-side fluid dynamics are also dependent on the method of air entrainment (plunging jet vs. spilling breaker, e.g., Yang et al. (2018)), and the spilling breakers in SOARS are likely to generate dynamic differences from the plunging sheets used previously (Callaghan et al., 2014; Forestieri et al., 2018). The fluid dynamics of each system will vary owing to the system dimensions and presence or absence of wind, influencing D_1 (Eq. 4).

3.5 Particle Number Flux Distributions

Emission fluxes of SSA in SOARS also decrease with increasing SST, but with a striking size-dependence. Size-resolved PNFDs at the lowest and highest SSTs (Figure 7a) reveal a crossover: SSA smaller than 0.6 µm are emitted at lower rates at high SSTs, while SSA larger than 0.75 µm show the opposite trend. Tri-modal fitting quantifies this divergence, where total number flux (F_N) for the Aitken and accumulation modes decreases by 82% and 58%, respectively, while supermicron F_N increases by more than a factor of three (Table S4). This size-dependent behaviour suggests that the mechanisms governing film drop production (predominantly submicron) and jet drop production (predominantly supermicron) respond differently to changes in SST. Linear regressions capture the Aitken and accumulation mode trends well ($R^2 \geq 0.99$), while the supermicron mode requires a quadratic fit, consistent with its non-monotonic SST dependence (Table 1, Eqs. 7–8). These regressions were evaluated separately for each experiment and for all measurements combined (Figure S9) to account for the limited number of temperature bins (n = 5).

https://doi.org/10.5194/egusphere-2026-2142
Preprint. Discussion started: 27 April 2026

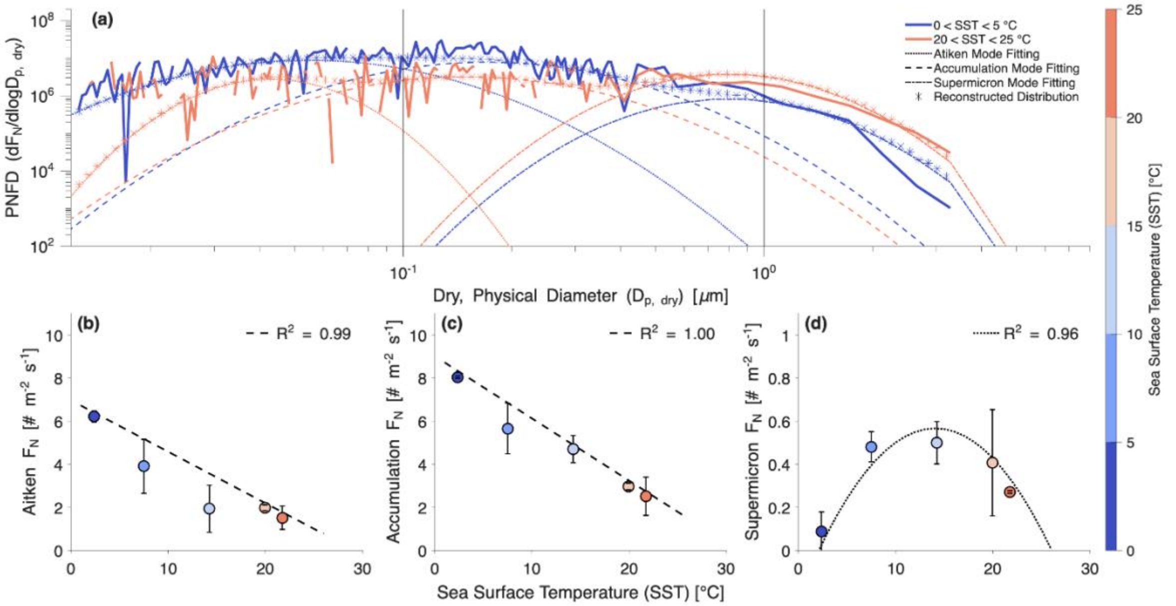

Figure 7: (a) Average PNFD for 2 °C and 23 °C. Each PNFD is decomposed into three log-normal modes and reconstructed. Weighted least squares linear (dashed lines) and quadratic (dotted lines) regressions of total number flux for the (b) Aitken, (c) accumulation, and (d) supermicron modes.

$$F_N = a_1 * SST + a_2, \tag{7}$$

$$F_N = b_1 * SST^2 + b_2 * SST + b_3, \tag{8}$$

Mode	**a_1**	**a_2**	**R^2**
Aitken	-2.39e5	6.73e6	0.99
Accumulation	-2.89e5	8.72e6	1.00
Coarse	-3.55e3	3.49e5	0.06
Total	-5.08e5	1.57e7	1.00

	b_1	**b_2**	**b_3**	**R^2**
Aitken	1.16e4	-5.00e5	7.32e6	1.00
Accumulation	1.81e3	-3.29e5	8.81e6	1.00
Coarse	-3.95e3	1.03e5	-1.09e5	0.96
Total	-3.26e3	-4.33e5	1.56e7	1.00

Table 1: Least squares regression and coefficients of determination for linear and quadratic fits to total number fluxes.

Aitken and accumulation mode SSA number flux SST dependencies exhibit trends well captured by both linear and quadratic regressions ($R^2 \geq 0.99$), while the SST dependence of supermicron SSA is captured by a quadratic regression. SSA number emissions are dominated by submicron SSA (Figure 7a), so a first-order SST dependency is recommended for computational efficiency for model integration. Further, a monotonically decreasing SST dependence for total SSA number flux agrees with previous estimates (Grythe et al., 2014; Lehahn et al., 2014; Markuszewski et al., 2024). This first-order relationship forms the basis of the temperature-dependent number flux correction factor (CF_N), developed in Section 3.6 for direct integration into ESMs.

To ensure compatibility with SSA modelling schemes that parameterize emissions by mass, the PNFDs and F_N values are converted to particle mass flux distributions (PMFDs) and total mass flux (F_M), assuming spherical particles and a density of 2.2 g cm^{-3} (Brock et al., 2019; Wu et al., 2020) (Figure S8, Figure S10). The mass flux results diverge markedly from the number flux results. Because particle mass scales with the cube of diameter, F_M is dominated by the largest SSA in each mode — particles whose emission rates increase with SST (Figure 7a, d). As a result, while the Aitken mode PMFD mirrors its PNFD counterpart, both the accumulation and supermicron mode PMFDs exhibit non-monotonic SST dependencies with maxima near 15 °C, resembling the supermicron PNFD behaviour. Note that these PMFD trends differ from the $dV/dlogD_{p,dry}$ curves in Figure 5f, which reflect steady-state concentrations rather than emission fluxes. The opposing SST dependencies of F_N and F_M — one monotonically decreasing, the other non-monotonic — necessitate separate correction factors for number and mass emissions in models. A temperature-dependent mass flux correction factor (CF_M) is developed alongside CF_N in Section 3.6.

3.6 Correction Factors (CFs) for Model Integration of SST Dependence

The uncertainties of simulated SSA in ESMs can be reduced by incorporating SST-dependent emission correction factors derived from the SOARS total number flux (CF_N) and mass flux (CF_M) measurements. Critically, these correction factors (Figure 8) are normalized to remove any dependence on absolute emission rates in SOARS, making them applicable to any SSA emission scheme. F_N at each SST is normalized by the average F_N at 14 ± 3 °C ($8 \pm 2 \times 10^6$ $\#_{SSA}$ m^{-2} s^{-1}), a reference temperature chosen to represent the annual SST range of the local seawater used in this study (Espinosa-Carreón et al., 2001). CF_M is generated through a parallel normalization of F_M at 14 ± 3 °C (0.034 ± 0.007 kg m^{-2} s^{-1}). CF_N and CF_M are represented by Eqs. 9 and 10, respectively:

$$CF_N = -0.064 * SST + 1.950, \quad (9)$$

$$CF_M = -0.006 * SST^2 + 0.152 * SST + -0.035, \quad (10)$$

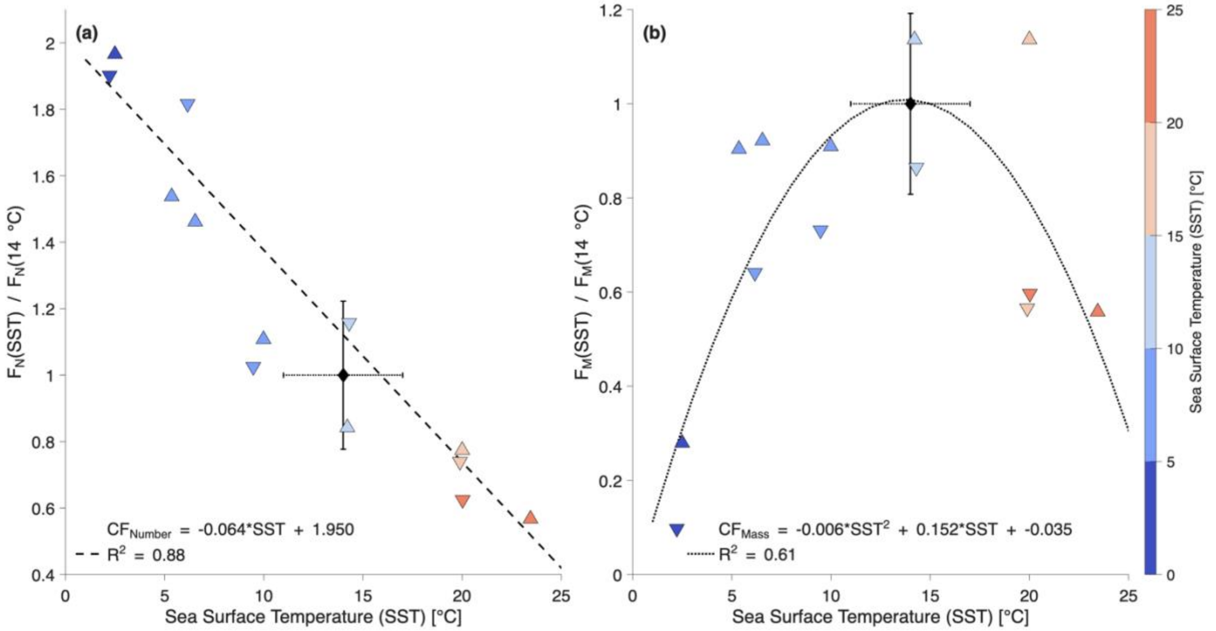

Figure 8: (a) Total number emission flux (F_N) and (b) total mass emission flux (F_M) as a function of SST, normalized by the average flux at 14 °C. The black diamond depicts flux at 14 °C, and the vertical error bars represent one standard deviation. The horizontal error bars represent the annual SST range of the coastal seawater sourced for this study.

Incorporating these correction factors into ESMs would substantially alter simulated SSA burdens, consistent with sensitivity analyses in previous work (Grythe et al., 2014; Jaeglé et al., 2011; Ovadnevaite et al., 2014; Sofiev et al., 2011). The magnitude of this impact is underscored by the fact that only half of the emission schemes that currently incorporate an SST dependence (Grythe et al., 2014; Jaeglé et al., 2011; Mårtensson et al., 2003; Salter et al., 2015) predict the correct sign. The other half simulate increasing SSA production with SST, the opposite of what is observed here. CF_M introduces an additional sensitivity at moderate SSTs, where small deviations from 15 °C will lead to large decreases in mass flux, a regime that encompasses much of the global ocean. Because Eqs. 9–10 are derived from SSA produced by realistic wind-wave interactions, they represent the most physically grounded SST correction factors currently available for ESM integration.

4 Conclusions

This is the first study to generate SSA through wind-wave interactions in controlled laboratory conditions under varied SSTs, using a comprehensive set of measurement techniques to probe the uncertain relationship between SST and SSA production. The results presented here incorporate measurements of whitecap fraction, subsurface bubble concentrations, steady-state SSA concentrations, and SSA emission fluxes to build a robust framework for characterizing the SST dependence of SSA.

Increasing SST in SOARS from 2 to 23 °C resulted in decreases of subsurface bubble concentrations (Figure 2b), total SSA number concentration (Figure 3), and SSA number emission flux (Figure 7) by factors of approximately 1.5, 3, and 4, respectively. These findings depend on realistic SSA production methods to corroborate previous estimates (Christiansen et al., 2019; Lehahn et al., 2014; Markuszewski et al., 2024; Nielsen and Bilde, 2020; Salter et al., 2014, 2015; Sellegri et al., 2023). Surface area and volume distributions (Figure 5) showed pronounced shifts as SST increased from 2 to 7 °C, suggesting the occurrence of a physicochemical or mechanistic shift. These results were consistent regardless of temperature hysteresis, indicating that the magnitude of SST is more important than the direction of change.

Subsequent work should pursue three avenues to better understand the temperature dependence of SSA production and the associated impacts. The first avenue should characterize the physicochemical mixing state of SSA at varied SSTs. Changes in mixing state are likely to accompany the shifts in production identified here and will directly depend on water composition. Aerosol composition shifts with temperature may explain more of the variability from previous studies.

The second avenue should seek to better characterize the SST-dependent SSA production at the single bubble level. We hypothesize that changes in the emission rate of SSA per bubble (E) or in surface bubble concentrations (n) are the cause of changes in SSA number, with estimates of E reaching a factor of 58 over a similar temperature range as this study (Nielsen and Bilde, 2020). Laboratory experiments, focused on the role of SST in determining single-bubble bursting characteristics, are currently missing from the literature and represent a knowledge gap that inhibits our understanding of interfacial fluxes.

The third avenue should focus on improved simulation of the SSA-SST dependence. Simulations should span the scales from direct numerical simulation of single-bubble processes to Earth system modelling using the CF_N and CF_M described here. Direct numerical simulation of single bubbles and bubble plumes can connect SST-dependencies across scales and improve the framework described in Sect. 3.1. Recent direct numerical simulation of breaking waves emphasizes the need to perform fine-resolution simulations (Yang et al., 2018), where SST-dependent systems should be a primary focus. Incorporation of the SOARS-based CFs could dramatically change simulated SSA production, especially under historical and projected scenarios in which SSTs are likely to change significantly. Improving simulated SSA dependence on SST is critical to understand associated changes in marine aerosol burdens, cloud condensation nuclei concentrations, and radiative forcing estimates.

Author Contributions

RJLIII and KAP conceptualized the study; RJLIII, JDH, MOA, and GBD created methodology for data collection and analysis; RJLIII, JDH, GBD, MDS, and GS curated software necessary for collection and analysis; JDH, RJLIII, GBD, and MDS performed data validation; JDH, RJLIII, and GBD performed formal analysis; RJLIII, JDH, JKH, KAK, and CH carried out the investigation; KAP, CL, GBD, MDS, and MOA provided resources; JDH, RJLIII, and JKH curated the data; RJLIII and

JDH prepared the manuscript with contributions from all authors; JDH and RJLIII visualized the data; RJLIII, KAK, CH, CL, MDS, GBD, MOA, and KAP supervised the project; RJLIII, CL, GBD, and KAP administered the project; KAP and GBD acquired funding.

Competing Interests

The authors declare that they have no conflicts of interest.

Data and Code Availability

All data and code needed to recreate these results will be stored in the University of California San Diego Library data archive with a publicly accessible DOI. This DOI will be constructed before final publication of the manuscript.

Acknowledgements

The authors acknowledge Joseph Mayer, Robert Klidy, and the team at the Marine Science Development Center at Scripps Institution of Oceanography for their dedication to the maintenance and operation of SOARS. The authors acknowledge meaningful conversations with James Bird, Duncan Watson-Parris, and Anne Barkley which helped extend the impact of this work.

Financial Support

This work was supported through the National Science Foundation (NSF) through the MRI grant (OCE- 1727039), the Center for Aerosol Impacts on Chemistry of the Environment (CAICE) grant (CHE-1801971), and support for MDS and GBD through grant (OCE-1924393).

References

Albrecht, B. A.: Aerosols, Cloud Microphysics, and Fractional Cloudiness, Science, 245, 1227–1230, 1989.

Amanatidis, S., Kim, C., Spielman, S. R., Lewis, G. S., Hering, S. V., and Flagan, R. C.: The Spider DMA: A miniature radial differential mobility analyzer, Aerosol Science and Technology, 54, 175–189, https://doi.org/10.1080/02786826.2019.1626974, 2020.

Amanatidis, S., Huang, Y., Pushpawela, B., Schulze, B. C., Kenseth, C. M., Ward, R. X., Seinfeld, J. H., Hering, S. V., and Flagan, R. C.: Efficacy of a portable, moderate-resolution, fast-scanning differential mobility analyzer for ambient aerosol size distribution measurements, Atmospheric Measurement Techniques, 14, 4507–4516, https://doi.org/10.5194/amt-14-4507-2021, 2021.

Andreas, E. L., Edson, J. B., Monahan, E. C., Rouault, M. P., and Smith, S. D.: The spray contribution to net evaporation from the sea: A review of recent progress, Boundary-Layer Meteorol, 72, 3–52, https://doi.org/10.1007/BF00712389, 1995.

Bird, J. C., de Ruiter, R., Courbin, L., and Stone, H. A.: Daughter bubble cascades produced by folding of ruptured thin films, Nature, 465, 759–762, https://doi.org/10.1038/nature09069, 2010.

Bowyer, P. A., Woolf, D. K., and Monahan, E. C.: Temperature dependence of the charge and aerosol production associated with a breaking wave in a whitecap simulation tank, Journal of Geophysical Research: Oceans, 95, 5313–5319, https://doi.org/10.1029/JC095iC04p05313, 1990.

Brasz, C. F., Bartlett, C. T., Walls, P. L. L., Flynn, E. G., Yu, Y. E., and Bird, J. C.: Minimum size for the top jet drop from a bursting bubble, Phys. Rev. Fluids, 3, 074001, https://doi.org/10.1103/PhysRevFluids.3.074001, 2018.

Brock, C. A., Williamson, C., Kupc, A., Froyd, K. D., Erdesz, F., Wagner, N., Richardson, M., Schwarz, J. P., Gao, R. S., Katich, J. M., Campuzano-Jost, P., Nault, B. A., Schroder, J. C., Jimenez, J. L., Weinzierl, B., Dollner, M., Bui, T., and Murphy, D. M.: Aerosol size distributions during the Atmospheric Tomography Mission (ATom): Methods, uncertainties, and data products, Atmospheric Measurement Techniques, 12, 3081–3099, https://doi.org/10.5194/amt-12-3081-2019, 2019.

Callaghan, A. H., Stokes, M. D., and Deane, G. B.: The effect of water temperature on air entrainment, bubble plumes, and surface foam in a laboratory breaking-wave analog, Journal of Geophysical Research: Oceans, 119, 7463–7482, https://doi.org/10.1002/2014JC010351, 2014.

Chang, H.-M., Vazquez, C. I., Shiu, R.-F., and Chin, W.-C.: Temperature Effects on Effluent Microgel Formation, Polymers, 14, 4870, https://doi.org/10.3390/polym14224870, 2022.

Christiansen, S., Salter, M. E., Gorokhova, E., Nguyen, Q. T., and Bilde, M.: Sea Spray Aerosol Formation: Laboratory Results on the Role of Air Entrainment, Water Temperature, and Phytoplankton Biomass, Environ. Sci. Technol., 53, 13107–13116, https://doi.org/10.1021/acs.est.9b04078, 2019.

Chu, W., Zhang, R., Jiang, X., Villermaux, E., and Wang, X.: Critical Role of Sea Spray Aerosol Production Pathways in Particulate Transfer Across the Sea-Air Interface, Journal of Geophysical Research: Atmospheres, 130, e2025JD044168, https://doi.org/10.1029/2025JD044168, 2025.

Collins, D. B., Zhao, D. F., Ruppel, M. J., Laskina, O., Grandquist, J. R., Modini, R. L., Stokes, M. D., Russell, L. M., Bertram, T. H., Grassian, V. H., Deane, G. B., and Prather, K. A.: Direct aerosol chemical composition measurements to evaluate the physicochemical differences between controlled sea spray aerosol generation schemes, Atmospheric Measurement Techniques, 7, 3667–3683, https://doi.org/10.5194/amt-7-3667-2014, 2014.

Crawford, G. B. and Farmer, D. M.: On the spatial distribution of ocean bubbles, Journal of Geophysical Research: Oceans, 92, 8231–8243, https://doi.org/10.1029/JC092iC08p08231, 1987.

Czerski, H.: An Inversion of Acoustical Attenuation Measurements to Deduce Bubble Populations, https://doi.org/10.1175/JTECH-D-11-00170.1, 2012.

Dall'Osto, M., Park, J., Lee, Y., Jung, J., Kim, J.-H., Yang, E. J., Beddows, D. C. S., Harrison, R. M., Sellegri, K., Skov, H., Massling, A., and Yoon, Y. J.: Arctic Sea Ice Melting Controls Sea Spray Aerosol Production, Environ. Sci. Technol., acs.est.5c13886, https://doi.org/10.1021/acs.est.5c13886, 2025.

DeMott, P. J., Hill, T. C. J., McCluskey, C. S., Prather, K. A., Collins, D. B., Sullivan, R. C., Ruppel, M. J., Mason, R. H., Irish, V. E., Lee, T., Hwang, C. Y., Rhee, T. S., Snider, J. R., McMeeking, G. R., Dhaniyala, S., Lewis, E. R., Wentzell, J. J.

B., Abbatt, J., Lee, C., Sultana, C. M., Ault, A. P., Axson, J. L., Martinez, M. D., Venero, I., Santos-Figueroa, G., Stokes, M. D., Deane, G. B., Mayol-Bracero, O. L., Grassian, V. H., Bertram, T. H., Bertram, A. K., Moffett, B. F., and Franc, G. D.: Sea spray aerosol as a unique source of ice nucleating particles, Proceedings of the National Academy of Sciences of the United States of America, 113, 5797–5803, https://doi.org/10.1073/pnas.1514034112, 2016.

Espinosa-Carreón, T. L., Gaxiola-Castro, G., Robles-Pacheco, J. M., and Nájera-Martínez, S.: Temperature, salinity, nutrients and chlorophyll a in coastal waters of the Southern California Bight, Ciencias Marinas, 27, 397–422, https://doi.org/10.7773/cm.v27i3.490, 2001.

Forestieri, S. D., Moore, K. A., Martinez Borrero, R., Wang, A., Stokes, M. D., and Cappa, C. D.: Temperature and Composition Dependence of Sea Spray Aerosol Production, Geophysical Research Letters, 45, 7218–7225, https://doi.org/10.1029/2018GL078193, 2018.

Foster, G. and Rahmstorf, S.: Global Warming Has Accelerated Significantly, Geophysical Research Letters, 53, e2025GL118804, https://doi.org/10.1029/2025GL118804, 2026.

Fuentes, E., Coe, H., Green, D., De Leeuw, G., and McFiggans, G.: Laboratory-generated primary marine aerosol via bubble-bursting and atomization, Atmospheric Measurement Techniques, 3, 141–162, https://doi.org/10.5194/amt-3-141-2010, 2010.

Gliß, J., Mortier, A., Schulz, M., Andrews, E., Balkanski, Y., Bauer, S. E., Benedictow, A. M. K., Bian, H., Checa-Garcia, R., Chin, M., Ginoux, P., Griesfeller, J. J., Heckel, A., Kipling, Z., Kirkevåg, A., Kokkola, H., Laj, P., Le Sager, P., Lund, M. T., Lund Myhre, C., Matsui, H., Myhre, G., Neubauer, D., van Noije, T., North, P., Olivié, D. J. L., Rémy, S., Sogacheva, L., Takemura, T., Tsigaridis, K., and Tsyro, S. G.: AeroCom phase III multi-model evaluation of the aerosol life cycle and optical properties using ground- and space-based remote sensing as well as surface in situ observations, Atmospheric Chemistry and Physics, 21, 87–128, https://doi.org/10.5194/acp-21-87-2021, 2021.

Grythe, H., Ström, J., Krejci, R., Quinn, P., and Stohl, A.: A review of sea-spray aerosol source functions using a large global set of sea salt aerosol concentration measurements, Atmospheric Chemistry and Physics, 14, 1277–1297, https://doi.org/10.5194/acp-14-1277-2014, 2014.

Hansen, J., Sato, M., Ruedy, R., Lo, K., Lea, D. W., and Medina-Elizade, M.: Global temperature change, Proceedings of the National Academy of Sciences, 103, 14288–14293, https://doi.org/10.1073/pnas.0606291103, 2006.

Haywood, J. and Boucher, O.: Estimates of the direct and indirect radiative forcing due to tropospheric aerosols: A review, Reviews of Geophysics, 38, 513–543, https://doi.org/10.1029/1999RG000078, 2000.

Hering, S. V., Lewis, G. S., Spielman, S. R., and Eiguren-Fernandez, A.: A MAGIC concept for self-sustained, water-based, ultrafine particle counting, Aerosol Science and Technology, 53, 63–72, https://doi.org/10.1080/02786826.2018.1538549, 2019.

Hu, J., Li, J., Tsona Tchinda, N., Song, Y., Xu, M., Li, K., and Du, L.: Underestimated role of sea surface temperature in sea spray aerosol formation and climate effects, npj Clim Atmos Sci, 7, 1–12, https://doi.org/10.1038/s41612-024-00823-x, 2024.

Intergovernmental Panel on Climate Change (IPCC) (Ed.): The Earth’s Energy Budget, Climate Feedbacks and Climate Sensitivity, in: Climate Change 2021 – The Physical Science Basis: Working Group I Contribution to the Sixth Assessment Report of the Intergovernmental Panel on Climate Change, Cambridge University Press, Cambridge, 923–1054, https://doi.org/10.1017/9781009157896.009, 2023.

Jaeglé, L., Quinn, P. K., Bates, T. S., Alexander, B., and Lin, J.-T.: Global distribution of sea salt aerosols: new constraints from in situ and remote sensing observations, Atmospheric Chemistry and Physics, 11, 3137–3157, https://doi.org/10.5194/acp-11-3137-2011, 2011.

Jia, N. and Zhao, D.: The Influence of Wind Speed and Sea States on Whitecap Coverage, J. Ocean Univ. China, 18, 282–292, https://doi.org/10.1007/s11802-019-3808-7, 2019.

Jiang, X., Rotily, L., Villermaux, E., and Wang, X.: Abyss Aerosols: Drop Production from Underwater Bubble Collisions, Phys. Rev. Lett., 133, 024001, https://doi.org/10.1103/PhysRevLett.133.024001, 2024.

Kay, J. E., Wall, C., Yettella, V., Medeiros, B., Hannay, C., Caldwell, P., and Bitz, C.: Global Climate Impacts of Fixing the Southern Ocean Shortwave Radiation Bias in the Community Earth System Model (CESM), Journal of Climate, https://doi.org/10.1175/JCLI-D-15-0358.1, 2016.

Kimble, K. A., Leibensperger, R. J. I., Lee, C., Harb, C., Pogue, E. A., Deane, G. B., Stokes, M. D., and Prather, K. A.: Wind-Driven Influence on Submicron Sea Spray Aerosol Chemical Mixing State, ACS EST Air, https://doi.org/10.1021/acsestair.5c00339, 2026.

de Leeuw, G., Andreas, E. L., Anguelova, M. D., Fairall, C. W., Lewis, E. R., O'Dowd, C., Schulz, M., and Schwartz, S. E.: Production flux of sea spray aerosol, Reviews of Geophysics, 49, https://doi.org/10.1029/2010RG000349, 2011.

Lehahn, Y., Koren, I., Rudich, Y., Bidle, K. D., Trainic, M., Flores, J. M., Sharoni, S., and Vardi, A.: Decoupling atmospheric and oceanic factors affecting aerosol loading over a cluster of mesoscale North Atlantic eddies, Geophysical Research Letters, 41, 4075–4081, https://doi.org/10.1002/2014GL059738, 2014.

Lewis, E. R. and Schwartz, S. E.: Sea Salt Aerosol Production Mechanisms, Methods, Measurements and Models, Washington DC, 2004.

Liu, H., Pei, X., Zhang, F., Song, Y., Kuang, B., Xu, Z., and Wang, Z.: Relative Humidity Dependence of Growth Factor and Real Refractive Index for Sea Salt/Malonic Acid Internally Mixed Aerosols, JGR Atmospheres, 128, e2022JD037579, https://doi.org/10.1029/2022JD037579, 2023.

Liu, M. and Yang, B.: Evaluation of Sea Surface Temperature-Dependent Whitecap Coverage Parameterizations Using In Situ Data, Ocean Sci. J., 57, 174–185, https://doi.org/10.1007/s12601-022-00060-4, 2022.

Liu, S., Liu, C. C., Froyd, K. D., Schill, G. P., Murphy, D. M., Bui, T. P., Dean-Day, J. M., Weinzierl, B., Dollner, M., Diskin, G. S., Chen, G., and Gao, R. S.: Sea spray aerosol concentration modulated by sea surface temperature, Proceedings of the National Academy of Sciences of the United States of America, 118, 3–8, https://doi.org/10.1073/pnas.2020583118, 2021.

Llovel, W. and Terray, L.: Observed southern upper-ocean warming over 2005–2014 and associated mechanisms, Environ. Res. Lett., 11, 124023, https://doi.org/10.1088/1748-9326/11/12/124023, 2016.

Lohmann, U. and Feichter, J.: Global indirect aerosol effects: a review, Atmospheric Chemistry and Physics, 5, 715–737, https://doi.org/10.5194/acp-5-715-2005, 2005.

Markuszewski, P., Nilsson, E. D., Zinke, J., Mårtensson, E. M., Salter, M., Makuch, P., Kitowska, M., Niedźwiecka-Wróbel, I., Drozdowska, V., Lis, D., Petelski, T., Ferrero, L., and Piskozub, J.: Multi-year gradient measurements of sea spray fluxes over the Baltic Sea and the North Atlantic Ocean, Atmospheric Chemistry and Physics, 24, 11227–11253, https://doi.org/10.5194/acp-24-11227-2024, 2024.

Mårtensson, E. M., Nilsson, E. D., de Leeuw, G., Cohen, L. H., and Hansson, H.-C.: Laboratory simulations and parameterization of the primary marine aerosol production, Journal of Geophysical Research: Atmospheres, 108, https://doi.org/10.1029/2002JD002263, 2003.

Mehta, S., Ortiz-Suslow, D. G., Smith, A. W., and Haus, B. K.: A Laboratory Investigation of Spume Generation in High Winds for Fresh and Seawater, Journal of Geophysical Research: Atmospheres, 124, 11297–11312, https://doi.org/10.1029/2019JD030928, 2019.

Moore, K. A., Alexander, S. P., Humphries, R. S., Jensen, J., Protat, A., Reeves, J. M., Sanchez, K. J., Kreidenweis, S. M., and DeMott, P. J.: Estimation of Sea Spray Aerosol Surface Area Over the Southern Ocean Using Scattering Measurements, Journal of Geophysical Research: Atmospheres, 127, e2022JD037009, https://doi.org/10.1029/2022JD037009, 2022.

Nielsen, L. S. and Bilde, M.: Exploring controlling factors for sea spray aerosol production: temperature, inorganic ions and organic surfactants, Tellus B: Chemical and Physical Meteorology, 72, 1–10, https://doi.org/10.1080/16000889.2020.1801305, 2020.

O’Dowd, C. D. and De Leeuw, G.: Marine aerosol production: a review of the current knowledge, Phil. Trans. R. Soc. A., 365, 1753–1774, https://doi.org/10.1098/rsta.2007.2043, 2007.

Orellana, M. V., Matrai, P. A., Leck, C., Rauschenberg, C. D., Lee, A. M., and Coz, E.: Marine microgels as a source of cloud condensation nuclei in the high Arctic, Proc. Natl. Acad. Sci. U.S.A., 108, 13612–13617, https://doi.org/10.1073/pnas.1102457108, 2011.

Orellana, M. V., Hansell, D. A., Matrai, P. A., and Leck, C.: Marine Polymer-Gels’ Relevance in the Atmosphere as Aerosols and CCN, Gels, 7, 185, https://doi.org/10.3390/gels7040185, 2021.

Ovadnevaite, J., Manders, A., de Leeuw, G., Ceburnis, D., Monahan, C., Partanen, A.-I., Korhonen, H., and O’Dowd, C. D.: A sea spray aerosol flux parameterization encapsulating wave state, Atmos. Chem. Phys., 14, 1837–1852, https://doi.org/10.5194/acp-14-1837-2014, 2014.

Peters, T. M. and Leith, D.: Concentration measurement and counting efficiency of the aerodynamic particle sizer 3321, Journal of Aerosol Science, 34, 627–634, https://doi.org/10.1016/S0021-8502(03)00030-2, 2003.

Pfeifer, S., Müller, T., Weinhold, K., Zikova, N., Martins dos Santos, S., Marinoni, A., Bischof, O. F., Kykal, C., Ries, L., Meinhardt, F., Aalto, P., Mihalopoulos, N., and Wiedensohler, A.: Intercomparison of 15 aerodynamic particle size spectrometers (APS 3321): uncertainties in particle sizing and number size distribution, Atmospheric Measurement Techniques, 9, 1545–1551, https://doi.org/10.5194/amt-9-1545-2016, 2016.

Phillips, V. T. J., DeMott, P. J., and Andronache, C.: An Empirical Parameterization of Heterogeneous Ice Nucleation for Multiple Chemical Species of Aerosol, https://doi.org/10.1175/2007JAS2546.1, 2008.

Prather, K. A., Bertram, T. H., Grassian, V. H., Deane, G. B., Stokes, M. D., DeMott, P. J., Aluwihare, L. I., Palenik, B. P., Azam, F., Seinfeld, J. H., Moffet, R. C., Molina, M. J., Cappa, C. D., Geiger, F. M., Roberts, G. C., Russell, L. M., Ault, A. P., Baltrusaitis, J., Collins, D. B., Corrigan, C. E., Cuadra-Rodriguez, L. A., Ebben, C. J., Forestieri, S. D., Guasco, T. L., Hersey, S. P., Kim, M. J., Lambert, W. F., Modini, R. L., Mui, W., Pedler, B. E., Ruppel, M. J., Ryder, O. S., Schoepp, N. G., Sullivan, R. C., and Zhao, D.: Bringing the ocean into the laboratory to probe the chemical complexity of sea spray aerosol, Proceedings of the National Academy of Sciences of the United States of America, 110, 7550–7555, https://doi.org/10.1073/pnas.1300262110, 2013.

Quinn, P. K., Collins, D. B., Grassian, V. H., Prather, K. A., and Bates, T. S.: Chemistry and Related Properties of Freshly Emitted Sea Spray Aerosol, Chemical Reviews, 115, 4383–4399, https://doi.org/10.1021/cr500713g, 2015.

Resplandy, L., Keeling, R. F., Eddebbar, Y., Brooks, M., Wang, R., Bopp, L., Long, M. C., Dunne, J. P., Koeve, W., and Oschlies, A.: Quantification of ocean heat uptake from changes in atmospheric O2 and CO2 composition, Sci Rep, 9, 20244, https://doi.org/10.1038/s41598-019-56490-z, 2019.

Russell, L. M., Moore, R. H., Burrows, S. M., and Quinn, P. K.: Ocean flux of salt, sulfate, and organic components to atmospheric aerosol, Earth-Science Reviews, 239, 104364, https://doi.org/10.1016/j.earscirev.2023.104364, 2023.

Saliba, G., Chen, C.-L., Lewis, S., Russell, L. M., Rivellini, L.-H., Lee, A. K. Y., Quinn, P. K., Bates, T. S., Haëntjens, N., Boss, E. S., Karp-Boss, L., Baetge, N., Carlson, C. A., and Behrenfeld, M. J.: Factors driving the seasonal and hourly variability of sea-spray aerosol number in the North Atlantic, Proceedings of the National Academy of Sciences, 116, 20309–20314, https://doi.org/10.1073/pnas.1907574116, 2019.

Salter, M. E., Nilsson, E. D., Butcher, A., and Bilde, M.: On the seawater temperature dependence of the sea spray aerosol generated by a continuous plunging jet, Journal of Geophysical Research: Atmospheres, 119, 9052–9072, https://doi.org/10.1002/2013JD021376, 2014.

Salter, M. E., Zieger, P., Acosta Navarro, J. C., Grythe, H., Kirkevåg, A., Rosati, B., Riipinen, I., and Nilsson, E. D.: An empirically derived inorganic sea spray source function incorporating sea surface temperature, Atmospheric Chemistry and Physics, 15, 11047–11066, https://doi.org/10.5194/acp-15-11047-2015, 2015.

Sellegri, K., Barthelmeß, T., Trueblood, J., Cristi, A., Freney, E., Rose, C., Barr, N., Harvey, M., Safi, K., Deppeler, S., Thompson, K., Dillon, W., Engel, A., and Law, C.: Quantified effect of seawater biogeochemistry on the temperature dependence of sea spray aerosol fluxes, Atmospheric Chemistry and Physics, 23, 12949–12964, https://doi.org/10.5194/acp-23-12949-2023, 2023.

Sofiev, M., Soares, J., Prank, M., de Leeuw, G., and Kukkonen, J.: A regional-to-global model of emission and transport of sea salt particles in the atmosphere, Journal of Geophysical Research: Atmospheres, 116, https://doi.org/10.1029/2010JD014713, 2011.

Sofieva, S., Asmi, E., Atanasova, N. S., Heikkinen, A. E., Vidal, E., Duplissy, J., Romantschuk, M., Kouznetsov, R., Kukkonen, J., Bamford, D. H., Hyvärinen, A.-P., and Sofiev, M.: Effects of temperature and salinity on bubble-bursting aerosol formation simulated with a bubble-generating chamber, Atmospheric Measurement Techniques, 15, 6201–6219, https://doi.org/10.5194/amt-15-6201-2022, 2022.

Song, A., Li, J., Tsona, N. T., and Du, L.: Parameterizations for sea spray aerosol production flux, Applied Geochemistry, 157, 105776, https://doi.org/10.1016/j.apgeochem.2023.105776, 2023.

Stokes, M. D., Deane, G. B., Prather, K., Bertram, T. H., Ruppel, M. J., Ryder, O. S., Brady, J. M., and Zhao, D.: A Marine Aerosol Reference Tank system as a breaking wave analogue for the production of foam and sea-spray aerosols, Atmospheric Measurement Techniques, 6, 1085–1094, https://doi.org/10.5194/amt-6-1085-2013, 2013.

Thorpe, S. A., Bowyer, P., and Woolf, D. K.: Some Factors Affecting the Size Distributions of Oceanic Bubbles, Journal of Physical Oceanography, 22, 382–389, 1992.

Twomey, S.: Cloud nucleation in the atmosphere and influence of nucleus concentration levels in atmospheric physics, The Journal of Physical Chemistry, 84, 1459–1463, https://doi.org/10.1021/j100449a006, 1980.

Vagle, S. and Farmer, D. M.: A comparison of four methods for bubble size and void fraction measurements, IEEE Journal of Oceanic Engineering, 23, 211–222, https://doi.org/10.1109/48.701193, 1998.

Verdugo, P.: Marine Microgels, Annu. Rev. Mar. Sci., 4, 375–400, https://doi.org/10.1146/annurev-marine-120709-142759, 2012.

Veron, F., Hopkins, C., Harrison, E. L., and Mueller, J. A.: Sea spray spume droplet production in high wind speeds, Geophysical Research Letters, 39, https://doi.org/10.1029/2012GL052603, 2012.

Von Der Weiden, S. L., Drewnick, F., and Borrmann, S.: Particle Loss Calculator - A new software tool for the assessment of the performance of aerosol inlet systems, Atmospheric Measurement Techniques, 2, 479–494, https://doi.org/10.5194/amt-2-479-2009, 2009.

Wang, X., Deane, G. B., Moore, K. A., Ryder, O. S., Stokes, M. D., Beall, C. M., Collins, D. B., Santander, M. V., Burrows, S. M., Sultana, C. M., and Prather, K. A.: The role of jet and film drops in controlling the mixing state of submicron sea spray aerosol particles, Proceedings of the National Academy of Sciences of the United States of America, 114, 6978–6983, https://doi.org/10.1073/pnas.1702420114, 2017.

Willis, J. K., Roemmich, D., and Cornuelle, B.: Interannual variability in upper ocean heat content, temperature, and thermosteric expansion on global scales, Journal of Geophysical Research: Oceans, 109, https://doi.org/10.1029/2003JC002260, 2004.

Wu, T., Zhang, F., Zhang, J., Jie, W., Zhang, Y., Wu, F., Li, L., Yan, J., Liu, X., Lu, X., Tan, H., Zhang, L., Wang, J., and Hu, A.: Beijing Climate Center Earth System Model version 1 (BCC-ESM1): model description and evaluation of aerosol simulations, Geoscientific Model Development, 13, 977–1005, https://doi.org/10.5194/gmd-13-977-2020, 2020.

Yang, Z., Deng, B.-Q., and Shen, L.: Direct numerical simulation of wind turbulence over breaking waves, Journal of Fluid Mechanics, 850, 120–155, https://doi.org/10.1017/jfm.2018.466, 2018.

Zábori, J., Matisāns, M., Krejci, R., Nilsson, E. D., and Ström, J.: Artificial primary marine aerosol production: a laboratory study with varying water temperature, salinity, and succinic acid concentration, Atmospheric Chemistry and Physics, 12, 10709–10724, https://doi.org/10.5194/acp-12-10709-2012, 2012.

Zinke, J., Nilsson, E. D., Zieger, P., and Salter, M. E.: The Effect of Seawater Salinity and Seawater Temperature on Sea Salt Aerosol Production, Journal of Geophysical Research: Atmospheres, 127, https://doi.org/10.1029/2021jd036005, 2022.